

# FURTHER INVESTIGATION OF MICRO HOVERING ROTOR AERODYNAMICS USING TIME ACCURATE COMPUTATIONS

Vinod K Lakshminarayan \*

James D. Baeder †

Alfred Gessow Rotorcraft Center  
Department of Aerospace Engineering  
University of Maryland  
College Park, MD 20742.

## Abstract

In this work, a compressible Reynolds Averaged Navier Stokes (RANS) code is used to further investigate the aerodynamics and flow physics of conventional hovering micro-rotor which operates at low Reynolds and Mach numbers. The current work also serves as a step towards developing a computational methodology that can serve as a predictive tool for a variety of conventional and unconventional rotary wing MAVs. Compared to previous work by the authors, where the calculations were done in the blade fixed frame, the present computations are done in a time accurate manner in the inertial frame, facilitated by the implementation of time-accurate preconditioning. The effect of leading edge geometry is investigated by looking at blunt and sharp profiles and comparing with experimental data. The thrust and power is reasonably well predicted for the sharp leading edge geometry. The performance prediction for the blunt leading edge geometry is slightly inferior because of discrepancy in the modeled geometry. Blunt leading edge geometry shows poorer performance compared to sharp leading edge geometry mainly because of large pressure drag acting at the blunt front. Blunt leading edge geometry also shows significant leading edge laminar separation bubble which results in complete separation near the tip. Flow visualization shows that the tip vortex flow-field is very complicated with the presence of secondary vortices and additional vortices formed due to separation near the trailing edge. The tip vortex profiles are reasonably well predicted, but the inadequacy of the turbulence model leads to some discrepancies during tip vortex formation. The swirl velocities for the micro-rotor is found to be significantly larger compared to full-scale rotor, which can be one of the reasons for additional power loss in the smaller scale rotors.

## Introduction

With the growing desire for efficient rotary wing MAV which typically operate between  $Re = 10^3 - 10^5$ , accurate predictions of low Mach, viscous dominated flows are in increasing demand. Because of the difficulties involved in experimentally studying MAV and the breakdown of analytical correlations for drag and boundary layer behavior for this Reynolds number range, accurate computational results are of critical importance to MAV research.

Low Reynolds number flow is well understood from a theoretical viscous flow perspective, however only limited computational validation of experimental data has been conducted in the Reynolds number range of 20,000 to 100,000. A major difficulty in the computational prediction of low Reynolds number aerodynamic flows is

the fact that the flow has a tendency to separate under relatively mild adverse pressure gradients. In addition, the possibility of isolated separation bubbles and laminar-turbulent transition can also cause significant turbulence modeling issues.

Unlike in fixed wing vehicles or even rotary wing vehicles in forward flight, the flow-field of hovering rotors is significantly influenced by the trailed wake system since it remains in the proximity of the rotor at all times. Therefore, an accurate representation of the tip vortex formation and evolution is essential in achieving high fidelity performance predictions of hovering MAV. The primary deficiency in this area is the lack of computational studies performed on near-field low Reynolds number tip vortices. An initial step taken by the authors of this work to study the flow physics of hovering micro-rotors using a compressible Reynolds Averaged Navier-Stokes (RANS)

\* Graduate Research Assistant, vinodkl@umd.edu

† Associate Professor, baeder@eng.umd.edu

solver showed encouraging results (Refs. 1, 2). The performance was predicted well and the flow-field agreed reasonably well with the experiments. However, there are certain shortcomings in these calculations arising as a result of the limitations in the previously implemented low Mach preconditioning. The preconditioning was applicable only to steady flows because of which the computations were done in the blade frame where source terms are added to the momentum equation to allow for the rotation. In this approach, a steady solution is sought relative to the rotor blade. However, the results indicated that the flow-field does not become stationary in time and therefore it is necessary to obtain a time accurate solution in order to capture the flow physics accurately. In addition, many unconventional MAV rotors such as ducted rotors, coaxial rotors, flapping rotors, cycloidal rotors etc. are inherently unsteady and needs to be solved in a time accurate manner.

With the recent implementation of the unsteady preconditioning, the present work will attempt to improve the analysis of the flow physics of conventional hovering micro-rotors. The results will be validated with the experimental performance and vortex structure data. The effect of leading edge geometry will be investigated by performing calculations on blunt and sharp leading edge profiles. Details of flow physics will be studied by looking at the separation and wake characteristics.

## Methodology

The computations are performed using the overset structured mesh solver OVERTURNS (Ref. 3). All the computations are performed in a time-accurate manner in the inertial frame of reference. The code solves the compressible RANS equations using a preconditioned dual-time scheme in the diagonalized approximate factorization framework, described by Buelow et al. (Ref. 4) and Pandya et al. (Ref. 5). The diagonal form of implicit approximate factorization method was originally developed by Pulliam and Chaussee (Ref. 6). The low Mach preconditioning is based on the one developed by Turkel (Ref. 7). The preconditioning is used not only to improve convergence but also to improve the accuracy. The inviscid terms are computed using a third order MUSCL scheme utilizing Koren's limiter with Roe's flux difference splitting and the viscous terms are computed using second order central differencing. The Spalart-Allmaras (Ref. 8) turbulence model is employed for the RANS closure. This one-equation model has the advantages of ease of implementation, computational efficiency and numerical stability. The production term in this eddy-viscosity model is modified (Ref. 3) to account for the reduction of turbulence in the vortex core due to flow rota-

tion effects. The downwash velocity in the bottom plane of the rotor can be significant. In order to account for this and to properly represent the inflow at the other far-field boundaries, the point-sink boundary condition approach of Srinivasan et al. (Ref. 9) is used.

## Results

### Isentropic Vortex Evolution

Evolution of a 2-D inviscid isentropic vortex in a low Mach free-stream is used to validate the implementation of the unsteady low Mach preconditioning. A  $41 \times 41$  uniform grid is used in the domain ( $0 \leq x \leq 10, 0 \leq y \leq 10$ ). Periodic conditions are assumed on all four grid boundaries. This is done in order to remove any effects of boundary inaccuracies and also to keep the domain small. Perturbations are added to the free-stream such that there is no entropy gradient in the flow-field.

Free-stream conditions are  $\rho = 1, u = u_\infty, v = 0$  and  $p = 1$ . The perturbations are given by:

$$(\delta u, \delta v) = \frac{\beta}{2\pi} e^{\frac{1-r^2}{2}} (-(y-y_0), (x-x_0)) \quad (1)$$

$$\rho = \left[ 1 - \frac{(\gamma-1)\beta^2}{8\gamma\pi} e^{1-r^2} \right]^{\frac{1}{\gamma-1}} \quad (2)$$

$$p = \rho^\gamma \quad (3)$$

where,  $\beta$  set as  $u_\infty$  is the vortex strength and  $r$  is the distance from the vortex center  $(x_0, y_0) = (5, 5)$ .

Two cases corresponding to  $u_\infty$  of 0.1 and 0.001 are studied. The corresponding free stream Mach numbers are respectively 0.0845 and 0.000845. In Pandya et al. (Ref. 5), an unsteady scale which depends on the unsteady length scale is used to define the preconditioning parameter. However, the unsteady length scale is quite arbitrary and cannot be defined easily for a practical problem. Therefore, in the present work, the authors use a different approach to control the preconditioning parameter by changing the pseudo time step ( $d\tau$ ). It can be shown that  $d\tau \rightarrow \infty$  is equivalent to no-preconditioning. As the value of  $d\tau$  is decreased, the effect of the preconditioning increases. However, a smaller value of  $d\tau$  would require sufficiently large number of sub-iterations to converge. Therefore, an appropriate value of  $d\tau$  has to be chosen.

To study the performance of the scheme with and without preconditioning, the sub-iteration convergence is studied for different physical time steps. The time step is characterized by  $CFL_u = \frac{u\Delta t}{\Delta x}$ , where  $u$  is the speed of propagation,  $\Delta t$  is the physical time step and  $\Delta x$  is the grid size. Figure 1 shows the residual convergence for the case  $M_\infty = 0.0845$  for two different time steps. For the preconditioning case, results were obtained for four differ-

ent values of  $d\tau$ . For  $CFL_u = 0.1$ , the no-preconditioning case shows the best convergence. The preconditioning cases show improving convergence as  $d\tau$  is increased and for  $d\tau = 100 dt$  the convergence becomes very similar to that of the no-preconditioning case. For the larger time step ( $CFL_u = 1.0$ ), the preconditioning cases with higher  $d\tau$  ( $10 dt$ ,  $100 dt$ ) show better convergence compared to the no-preconditioning case.

Figure 2 shows similar plots for the case  $M_\infty = 0.000845$ ; the advantages of the low Mach preconditioning can be clearly seen at the speed of  $u_\infty = 0.001$ . For this case, the no-preconditioning case shows very poor convergence for both the time steps. On the other hand, the preconditioning cases show good convergence. As a general trend, higher pseudo time step shows better convergence. It has to be mentioned here that for all cases when the time step was made very large, the convergence was similar to that of the no-preconditioning case. Therefore from the convergence point of view,  $d\tau = 100 dt$  seems to be a good choice. However, practical computations do not require that the sub-iterations be converged to machine zero. Typically, the residue is converged to 3 to 4 orders of magnitude or the number of sub-iterations is fixed to a value, typically 20. By looking at the convergence of various cases in the first 20 sub-iterations, it can be seen that the preconditioning cases with  $d\tau = dt$ ,  $10 dt$  and  $100 dt$  show equally good results, with the residues dropping by 3 to 4 orders of magnitude for all the cases. Therefore, the choice of  $d\tau$  cannot be determined just by looking at the convergence.

Figure 3 shows the vertical velocity profile along a line cut through the center of the vortex at  $t = 10$ . The results are obtained with a time step of  $CFL_u = 0.1$  and using 20 sub-iterations. The plot also shows the exact solution. For both the speeds, the preconditioning with smaller  $d\tau$  has lower dissipation. However,  $d\tau = 0.1 dt$  case is not converged sufficiently for both the cases. The no-preconditioning case is more dissipative compared to the preconditioning cases for  $u_\infty = 0.1$ . For  $u_\infty = 0.001$ , the no-preconditioning case does not converge and therefore is not plotted. Clearly,  $d\tau = dt$  is seen to give the best result and therefore can be considered the optimum choice. This value of  $d\tau$  will be used for all the following calculations.

## Hovering Rotor Validation

With the validation of low Mach preconditioning for a simple low speed 2-D vortex evolution case, the extension is made to the rotor case by exploring the experimental results obtained by Ramasamy et al. (Ref. 10) on a two-bladed hovering rotor at a tip Reynolds number of 32,400, tip Mach number of 0.08 and a wing aspect ratio of 4.39. The resulting rotor solidity is 0.145. The

untwisted rectangular blades uses a 3.3% curvature circular arc airfoil with a thickness of 3.7%. The baseline section has a blunt leading as well as trailing edge. Experiments were also performed on sections which were slightly different from the baseline section, one of them is a section with sharp leading edge and trailing edge (SLT). Performance data is available at various collective angles. High resolution flow visualization and particle image velocimetry (PIV) flow-field data is available for the case with collective angle of  $12^\circ$  using the baseline sectional profile.

Computations are performed on rotor blades with two different sectional profiles, see Fig. 4. One of them has a blunt leading edge similar to the baseline experimental section but with a sharp trailing edge (BLE). Computations with a blunt trailing edge are not performed because of the restrictions imposed by the C-type grid. However, in the past, researchers have shown that the trailing edge geometry has little effect on the lift and drag of thin wings/blades at low Reynolds numbers (Refs. 11–14). Therefore, computational results obtained using the BLE section should be comparable with that of experiments using the baseline section. The other section for which computational results were obtained has sharp leading and trailing edges with slight rounding at the leading edge (SLE) and is very similar to the experimental SLT section.

A two mesh overset system with a body conforming blade mesh and a cylindrical background mesh is used for the computations. A hole-cutting technique is used to blank out the portion of the background mesh that overlaps with the blade mesh. Information is exchanged from one grid to the other by means of interpolation. For  $12^\circ$  collective setting cases, where the flow-field is compared with the experiments, computations are performed on a fine mesh with the blade mesh having  $267 \times 185 \times 99$  points in the streamwise, spanwise and normal directions respectively and the background cylindrical mesh having  $127 \times 186 \times 198$  points in the azimuthal, radial and vertical directions respectively, Fig. 5. In the most refined regions, the background mesh has a grid spacing of 0.02 chords in both the radial and the vertical directions. Along the azimuthal direction, a grid plane is spaced every  $1.5^\circ$ . For all other collective settings, where only performance data is compared, computations are performed on a coarser mesh obtained by leaving out every other point in the spanwise and normal direction. The chosen time-steps corresponds to  $0.125^\circ$  of azimuth for the fine mesh and  $0.25^\circ$  of azimuth for the coarse mesh calculations.

## Performance Comparison

Figure 6(a) compares the computed performance with the experimentally measured values (Ref. 10). It can be seen that the computed performance for the SLE geometry shows good agreement with the experimental results for the SLT geometry, with the exception of a slight under-prediction of power at higher thrust levels, thereby validating the current computational study. It should be noted that the only difference between the experimental and the computational sectional profile is the slight rounding of the modeled geometry. It should also be mentioned here that a study was done to see the effect of rounding by slightly changing the leading edge curvature and the results did not show much variation. Therefore, the effect of leading edge rounding can be considered negligible.

The experimental results using the baseline geometry showed degraded performance at all thrust levels compared to the sharp leading edge geometry. The reason for this will be understood in the following sections. Corresponding to the experiment, the computed power for the BLE geometry is higher than that of the SLE geometry. However, the computed performance for this case shows poorer comparison with the measured baseline case values, as opposed to the computed and measured values for the sharp leading edge geometry. The predicted performance is slightly better than the measured values at all thrust levels. The reason for this discrepancy could arise mainly due to the difference in modeled trailing edge geometry which can result in slightly altered separation characteristics.

Figure 6(b) shows the comparison of figure of merit ( $FM$ ) versus thrust coefficient ( $C_T$ ). Again it can be seen that the computed results for the sharp leading edge geometry compare better with the corresponding experimental results as opposed to those for the blunt leading edge geometry. Looking at the computational results, it can be seen that while a blunt leading edge profile achieves a maximum  $FM$  of about 0.5, the sharp leading edge profile attains a maximum  $FM$  greater than 0.55. The maximum  $FM$  achieved in the experiments were slightly lower. The maximum  $FM$  is achieved at a thrust level of about 0.015 – 0.02 ( $C_T/\sigma \approx 0.12$ ) for both the geometries.

Figure 6 also shows the performance results obtained using fine meshes for the  $12^\circ$  collective setting. The results are comparable to the coarse mesh results. This shows grid convergence in the performance data.

## Blade Surface Streamlines

Separation patterns on the blade surfaces are used to highlight some of the differences resulting from the BLE and SLE geometries. Figure 7 shows the surface streamlines

on the blades for  $12^\circ$  collective setting for both BLE and SLE geometries. The results shown are obtained for the fine mesh calculations. For the SLE geometry, most of the flow is attached to at least the 80% chord position. However, the inboard stations show a small portion of leading edge separation which reattaches with fairly strong radial cross-flow. As a result, the downstream separation appears slightly delayed inboard. In contrast, the BLE geometry results in a leading edge separation that increases in chordwise extent as one goes towards the tip, with the flow completely separating at the tip. The reattachment downstream of the leading edge separation bubble then seems to extend to almost the same positions as for the SLE geometry. However, the amount of crossflow seems a little bit smaller.

## Spanwise Loading Distributions

The differences in the performance of the BLE and SLE geometries can be better understood by looking at the spanwise loading distributions. Figure 8(a) shows the spanwise thrust distribution for  $12^\circ$  collective setting for both BLE and SLE geometries. The distribution for both the geometries are comparable through most of the span except near the tip. However, the spanwise power distribution for both the cases, shown in Fig. 8(b), is similar only in the inboard regions. Blunt leading edge geometry results show higher power distribution at most of the span locations.

Isolating the power into components due to the viscous force (viscous power,  $C_{Q_v}$ ) and the pressure force (pressure power,  $C_{Q_p}$ ) can provide a better understanding of the reason for the disparities between the power distributions of the BLE and SLE geometries. When the flow is attached, the contribution due to the viscous and pressure forces are a first order approximation of the profile and induced components of power, respectively. However, for the present cases, especially for the BLE geometry case where there is significant separation, the profile and induced power needs to be defined more appropriately. Figure 8(c) and Fig. 8(d), respectively show the spanwise distribution of viscous and pressure power. From the figures, it is seen that in contrast to the total power, the viscous power distribution for the BLE geometry case is lower than that from the SLE geometry at all span locations. The reason for this is that when there is separated flow the skin friction is actually in the upstream direction, which lowers the skin friction drag. The distribution of the pressure component of power can be seen to be very similar to that of the total power. Since the viscous component is about an order of magnitude smaller than the pressure component, the disparities in the total powers of the BLE and SLE geometries arises mainly from the differences in the pressure components and the reason for

this dissemblance will be understood better when looking at the blade pressure distributions at different spanwise stations.

Apart from the spanwise thrust and power distributions, the spanwise lift distribution was also inspected. It was seen that the sectional lift coefficient was almost constant along the span, with a value of about 0.7 ( $\approx \frac{6C_L}{\sigma}$ ), for both the BLE and SLE geometries. This is a surprising result for an untwisted blade, because typically in a full-scale rotor one needs to provide twist to achieve constant lift coefficient throughout the span.

## Blade Pressure Distributions

A better understanding of the spanwise distributions of thrust and power can be obtained by looking at surface pressure plots at selected spanwise stations. Figure 9 shows the chordwise surface pressure distribution for the BLE and SLE geometries at  $12^\circ$  collective setting at four spanwise locations. The distribution for the SLE geometry do not show much variation with span, whereas those for the BLE geometry vary significantly with span, especially in the outboard regions because of the leading edge separation. The effect of the laminar separation bubble can be seen at the  $0.6R$  and  $0.8R$  span locations for the BLE geometry, where the pressure distributions becomes relatively constant near the leading edge. At  $0.95R$  span location, where the flow is completely separated, the pressure distribution on the upper surface can be seen to be wavy for the BLE geometry.

Comparing the chordwise pressure distributions for the BLE and SLE geometries, especially at the inboard locations, one observes that the distributions are different near the leading edge, whereas they are comparable near the trailing edge. This is as expected, because the BLE and SLE geometries differ only at the leading edge while being exactly similar at the trailing edge. The BLE geometry results in a larger suction peak which occurs at an earlier chordwise location compared to that for the SLE geometry.

Figure 10 shows the variation of surface pressure along the vertical direction at the same four spanwise locations for the BLE and SLE geometries at  $12^\circ$  collective setting. The surface pressures proceed in a clockwise manner around both geometries at all four spanwise locations, except right near the suction peaks at the leading edge (both at the top and bottom for the BLE geometry case). The area enclosed by the curve gives the sectional pressure drag coefficient. Clearly, the pressure drag for the BLE geometry is higher than that for the SLE geometry and the difference mainly occurs near the maximum  $z/c$  location which corresponds to the regions near the leading edge. The high pressure region created near the leading edge due to stagnating flow generates significant

amount of pressure drag for the BLE geometry case. A small contribution to the pressure drag also comes from the reduction in suction peak due to the leading edge laminar separation bubble.

## Sectional Flow Contours

In order to attain a better understanding of the separation, spanwise contours of eddy viscosity for the BLE and the SLE geometries at  $12^\circ$  collective setting are plotted in Figs. 11, 12, 13 and 14. At  $0.4R$  station there is little difference between the contours for the two geometry, but at that station the leading edge separation bubble for the BLE geometry is very small. The really high values of eddy viscosity are concentrated in the separated regions near the trailing edge and in the very near wake. The wake also seems to show the typical shear layer instabilities for low Reynolds number flow. By the  $0.6R$  station, the separation is more pronounced for the BLE geometry in the leading edge region; as a result, the BLE results do show a movement forward for the beginning of the growth in eddy viscosity. The region of higher eddy viscosity has grown slightly larger near the trailing edge for both geometries with clear shear layer instability. By the  $0.8R$  location, there is now a region of high eddy viscosity near the leading edge region for the BLE geometry that connects to the high eddy viscosity region near the trailing edge. It appears that the shear layer instability in the wake region has become somewhat damped for both the cases but even more so for the BLE geometry case. At the  $0.95R$  station there is clearly a relatively massively separated flow region that extends over nearly the whole chord of the cross section for the BLE geometry case, resulting in a large volume of high eddy viscosity flow.

Figures 15 and 16 show radial velocity contours along with streamlines at spanwise locations of  $0.4R$  and  $0.8R$ , respectively. The plots show similar separation features as those observed in the contours of eddy viscosity. It is interesting to note that in the regions of flow separation, the radial flow component of velocity is very strong as compared to the regions outside. This may result in the transport of eddy viscosity from within the leading edge separation bubble towards the tip, further elevating the level of eddy viscosity in the tip region.

## Flow-field Visualizations

Next, qualitative features in the flow-field are examined. Figure 17 shows iso-surfaces of the so-called  $q$ -criterion (Ref. 15) near the blade surface for  $12^\circ$  collective setting using both BLE and SLE geometry. While the flow is smooth near the tip of the SLE geometry, numerous vortical structures can be seen on the top of the BLE geometry blade due to flow separation. These structures can also

be seen in Fig. 18(a), which shows the streamwise vorticity contours. Looking at the tip vortex, for both the geometries, it is evident that the tip vortex flow-field is extremely complicated because of the presence of a variety of secondary structures near the blade tip. The origin of these structures can be discerned from Fig. 18. While initial traces of the tip vortex can be seen slightly upstream of the quarter-chord point, secondary vortices originate from the leading edge as well as from the separation of the crossflow boundary layer rolling over the rounded tip. In addition to the secondary vortices, a large number of additional vortical structures are found near the trailing edge of the blade over most of the span for both cases as seen from Fig. 18, more clearly seen for the SLE geometry. Similar vortical structures can be seen even in the experimental flow visualization (Ref. 10) shown in Fig. 19. These structures are formed as a result of flow separation near the blade trailing edge. Within a short distance downstream of the trailing edge, these structures appear to have merged with the tip vortex (as seen from the coherent iso-surface in Fig. 17).

Figure 20 shows the iso-surface of  $q$ -criterion in the entire flow-field for the BLE geometry at  $12^\circ$  collective setting. The resolution of the tip vortex until 3 blade passages is clearly evident. Beyond this wake-age, the background mesh becomes too coarse to accurately represent the details of the tip vortex. An interesting feature revealed from this figure is the fact that while the tip vortex is smooth initially, it seems to get twisted near the first blade passage. This is because of the fact that it is embedded in a highly strained field due to the presence of the evolving tip vortex (note that the vertical convection of the tip vortex is relatively low before the first pass as has been well documented (Refs. 16, 17)) and other near-blade structures. It is also seen that after the first pass, the vortex becomes wavy along its axis, thus suggesting slight instability. Interestingly, such an instability was observed experimentally even for a full-scale rotor (Ref. 16). It should be mentioned here that the corresponding iso-surface for the SLE geometry at  $12^\circ$  collective setting is not too different from Fig. 20.

Further evidence of the interaction between different turns of the tip vortex can be seen in Fig. 21(a), in which vorticity magnitude contours are shown along a  $0^\circ$  azimuthal plane of the background mesh. The tip vortex, after its first blade passage, is seen to interact with the in-board wake as well as the second blade passage, both of which introduce a strain-field. The experimental flow visualization (Ref. 10) plotted in Fig. 21(b) is qualitatively similar to the computed flow-field and shows similar interactions.

## Wake Trajectory

Figure 22 shows the computed wake trajectory for the BLE geometry at  $12^\circ$  collective setting. The radial contraction of the wake with azimuth is plotted in Fig. 22(a). The instability in the wake after the first blade passage (discussed before) can be seen in the form of wiggles after  $180^\circ$  azimuth. Additionally, the contraction rate is seen to decrease after the first blade passage at  $180^\circ$  azimuth as a result of the interaction of the tip vortex before the first blade passage with the tip vortex after the blade passage. The blade passage effect is also seen in the vertical convection of the wake, see Fig. 22(b). After the blade passage, the vertical convection rate increases because of increased inflow. Figure 22(c) shows the spatial location of the wake. It can be seen that the wake contracts to less than  $0.8R$  and is not too different from that observed for full scale rotors (Ref. 16). Again, the wake trajectory for the SLE geometry is not too different from that of the BLE geometry.

## Vortex Structure Comparison

Experimental data (Ref. 10) can be used to quantitatively validate the initial development and evolution of the tip vortex structure. Figures 23, 24 and 25 show the comparison of swirl velocity, axial velocity and streamwise vorticity profiles, respectively along a line passing through the center of the tip vortex at different wake ages. The computational results are obtained for the BLE geometry at  $12^\circ$  collective setting, while the experimental results are for the baseline geometry at the same collective setting. It should be noted that the axial deficit in the core of the vortex is very large and is most likely due to the dominance of viscous forces for these small scale micro-rotors. In general, there is a good agreement between the computational and the experimental results. However, at all azimuth locations, the peak swirl velocity and peak axial deficit are over-predicted, whereas peak vorticity is under-predicted. The core radius, defined as half the distance between the peak-to-peak swirl velocity is also over-predicted. However, the rate of core growth and the rate of peak swirl decay is predicted accurately, see Fig. 26, indicating that the inconsistency mainly arises during tip vortex formation, while the tip vortex evolution is well resolved.

There are two possible reasons for the discrepancy in the tip vortex formation. The main reason could be due to the inadequacy of the Spalart-Allmaras turbulence model in a non-isotropic environment such as those found near the regions of tip vortex formation. The second reason for the discrepancy could be due to under-resolution of the tip vortex formation because of insufficient mesh resolution near the blade tip. It should be noted that the

vortex profiles for the SLE geometry is very similar to the BLE geometry. There is some dissimilarity in the axial velocity profiles, however, the differences are not too large. Therefore, it is safe to assume that the difference between the BLE and the baseline geometry do not contribute to the differences in the computed and measured vortex profiles. It might be worthwhile to examine this issue using a DES approach in the tip region.

### Average Velocity Profiles in Wake

The sectional drag for low Reynolds number airfoils is much larger than that at high Reynolds number and may alter the induced velocities in the rotor wake for small scale micro-rotors. Figure 27 shows the radial variation of various components of velocity averaged in the azimuthal direction. The variation is shown at different planes below the rotor. It should be noted that the results shown at  $z = 0$  are obtained by averaging those at  $z = 0.1c$  and  $z = -0.1c$  (to minimize influence of the rotor blade). The velocities are non-dimensionalized by the tip speed. The peak magnitude of the radial velocity reaches about 15% of the tip speed in the plane of the rotor and it occurs near the tip of the blade. As one moves away from the rotor, the radial component becomes weaker and the location of peak radial velocity moves inboard as a result of wake contraction. Correspondingly, the location of peak swirl velocity and peak inflow also move inboard. The average magnitude of swirl velocity in the wake region remains fairly constant at about 5 – 6% of the tip speed at all distances from the blade, with the peak reaching about 10 – 12% of the tip speed. These values are significantly larger as compared to those for a full scale rotor. A sample result for a full scale rotor is plotted in Fig. 28. The computations were done on a 2-bladed rotor with an aspect ratio of 6. The rotor operates at a tip Reynolds number of  $1.6 \times 10^6$  and a tip Mach number of 0.387. The thrust level for the full scale rotor is about 0.005 compared to the thrust of 0.0167 for the micro-rotor. As a result, the inflow for the full-scale rotor is about half the value as that of the micro-rotor. The swirl velocity, however is only about one-fourth of that for the micro-rotor. The larger swirl velocity can be one of the reasons for additional power loss in micro scale rotors. Note that, similar magnitude of swirl velocity component was seen even for the SLE geometry.

### Summary and Conclusions

A compressible Reynolds Averaged Navier Stokes (RANS) solver was extended to perform time accurate computations at low Reynolds and Mach number flow regime by implementing a time accurate preconditioner.

The implementation of the time accurate preconditioner was validated using a model case of low speed evolution of 2-D inviscid isentropic vortex. Use of low Mach preconditioning showed better convergence compared to the no-preconditioning case, especially at very low speeds and higher time step. The preconditioning parameter was controlled by varying the pseudo time step. The value of  $d\tau = dt$  was found to be optimum in terms of convergence and accuracy.

The solver was further applied to simulate hovering rotor operating at low Reynolds and Mach number. Two different leading edge geometries (blunt and sharp leading edge) for the blade section were studied. The computations were validated with experimentally measured performance data and also with tip vortex data. Additionally, the flow physics of the hovering micro-rotor was looked in detail.

The results of this investigation demonstrated the capability of using time accurate compressible RANS solver to study aerodynamics of conventional hovering micro-rotors. As a continuing work, the methodology will be used to investigate aerodynamics of unconventional micro-rotor configurations. Coaxial rotor configuration in full-scale has been studied by the current authors (Ref. 18) and therefore as a first step, aerodynamics of coaxial rotor in micro-scale will be studied. The current methodology can also be used for designing a better blade for micro-rotors, which will help in improving the aerodynamic efficiency.

The following are some specific conclusions from the present work :

1. The performance of the sharp leading and trailing edge geometry showed good comparison with the experimental data. However, the performance for the blunt leading edge geometry showed poorer comparison with the corresponding experiments. The discrepancy was attributed to the difference in the modeled trailing edge profile.
2. The performance of the sharp leading edge geometry was better compared to that of blunt leading edge geometry. The total thrust produced by both the geometries were similar, however, the blunt geometry required larger power. The reason for this was found to be mainly because of the pressure drag created by the near stagnation pressure close to the blunt leading edge.
3. A small contribution to the additional power for the BLE geometry case also comes from the presence of significant leading edge separation bubble for the blunt leading edge geometry, which increased in chordwise extent as one goes towards the tip, eventually leading to complete separation near the tip.

4. Even though the sectional thrust values were comparable, the sectional chordwise pressure distribution for the two geometries were different near the leading edge even at the inboard portions of the blade. The blunt leading edge geometry had larger suction peak which occurred at an earlier chordwise location. In the outboard regions, the leading edge separation bubble of the blunt leading edge geometry resulted in a region of constant pressure near the leading edge, whereas the pressure distribution for the sharp leading edge geometry did not show much variation with the spanwise location.
5. The sectional contours of eddy viscosity showed larger turbulence in separated regions and in the very near wake for both the geometries. In the separated regions, the radial velocity was also larger and was directed towards the tip of the blade. The contour plots showed shear layer instabilities in the wake, which are typical for low Reynolds number flows.
6. Flow visualization showed that the tip vortex flow field is very complicated with the presence of secondary vortices. Additional vortices were found near the trailing edge of the blade over most of the span, a feature which was observed even in the experiments.
7. Tip vortex was resolved for three blade passages. The tip vortex formed on the micro-rotor blade was observed to interact with secondary vortices early in its development along the chord. After the first passage of the tip vortex under the blade, the vortex experienced some destabilization as it was influenced by the strain field from both the blade and the inboard wake sheet.
8. Wake trajectory showed that the wake contracts to about  $0.75R$ , which is similar to the wake contraction for a full-scale rotor. The effect of blade passage was seen as an increase in the vertical convection rate and a decrease in the radial contraction rate. The instabilities in the wake after the blade passage showed as oscillations in the radial location of the wake.
9. Tip vortex profiles compared reasonably well with the experiments. The peak swirl velocity and axial deficit along the vortex center and the vortex core radius were over-predicted at all wake ages, whereas the peak vorticity was under-predicted at all wake ages. The discrepancy was found to be caused during the tip vortex formation and the inadequacy of the Spalart-Allmaras turbulence model in non-isotropic environment could be the main reason for the disparity.
10. The radial variation of azimuthal average of various components of velocities were plotted at different planes below the rotor. The radial component of velocity was seen to decrease with the distance from the rotor, whereas the swirl velocity and the inflow velocity remained constant and increased, respectively. The swirl velocity component was found to be significantly larger compared to a full-scale rotor and could lead to significant power losses.

## Acknowledgments

This work is sponsored by the Army Research Office Contract MURI ARMY-W911NF0410176. Opinions, interpretations, conclusions, and recommendations are those of the authors and are not necessarily endorsed by the United States Government. The authors would like to thank the Technical Monitor Dr. Tom Doligalski and the MURI review team for their encouragement and support.

## References

- <sup>1</sup>Lakshminarayan, V. K., Bush, B. L., Duraisamy, K. and Baeder, J. D., "Computational Investigation of Micro Hovering Rotor Aerodynamics," *24<sup>th</sup> AIAA Applied Aerodynamics Conference*, San Francisco, CA, June 2006.
- <sup>2</sup>Lakshminarayan, V. K., and Baeder, J. D., "Computational Investigation of Micro Hovering Rotor Aerodynamics," *Proceedings of the American Helicopter Society International Specialists' Meeting on Unmanned Rotorcraft*, Phoenix, AZ, January 2007.
- <sup>3</sup>Duraisamy, K., "Studies in Tip Vortex Formation, Evolution and Control," *PhD dissertation, Department of Aerospace Engineering, University of Maryland at College Park*, 2005.
- <sup>4</sup>Buelow P. E. O., Schwer D. A., Feng J. and Merkle C. L. "A Preconditioned Dual-Time, Diagonalized ADI scheme for Unsteady Computations," *13<sup>th</sup> AIAA Computational Fluid Dynamics Conference, AIAA paper 97-2101*, Snowmass Village, CO, July 1997.
- <sup>5</sup>Pandya, S. A., Venkateswaran, S. and Pulliam, T. H. "Implementation of Preconditioned Dual-Time Procedures in OVERFLOW," *41<sup>st</sup> AIAA Aerospace Sciences Meeting and Exhibit, AIAA paper 2003-0072*, Reno, NV, January 2003.
- <sup>6</sup>Pulliam, T. H. and Chaussee, D. S. "A diagonal Form of an Implicit Approximate Factorization Algorithm," *Journal of Computational Physics*, Vol. 39, 1981, pp. 347–363.

<sup>7</sup>Turkel, E., "Preconditioning Techniques in Computational Fluid Dynamics," *Annual Review of Fluid Mechanics*, Vol. 31, January 1999, pp. 385–416.

<sup>8</sup>Spalart, P. R. and Allmaras, S. R., "A One Equation Turbulence Model for Aerodynamics Flow," *30<sup>th</sup> AIAA Aerospace Sciences Meeting and Exhibit, AIAA Paper 92-0439*, Reno, NV, 1992.

<sup>9</sup>Srinivasan, G. R., and Baeder, J. D., "TURNS: A Free-wake Euler/ Navier-Stokes Numerical method for Helicopter Rotors," *AIAA Journal*, Vol. 31, No. 5, May 1993, pp. 959–962.

<sup>10</sup>Ramasamy, M., Johnson, B., and Leishman, J. G., "Toward Understanding the Aerodynamic Efficiency of a Hovering Micro-Rotor," *Proceedings of the American Helicopter Society International Specialists' Meeting on Unmanned Rotorcraft*, Phoenix, AZ, January 2007.

<sup>11</sup>Mueller, T. J., "Aerodynamic Measurements at Low Reynolds Numbers for Fixed Wing Micro-Air Vehicles," Presented at the RTO AVT/VKI Special course on Development and Operation of UAVs for Military and Civil Applications, VKI, Belgium, September 1999.

<sup>12</sup>Mueller, T. J., and Batill, S. M., "Experimental Studies of Separation on a Two-Dimensional Airfoil at Low Reynolds Numbers," *AIAA Journal*, Vol. 20, No. 4, April 1982, pp. 456–463.

<sup>13</sup>Mueller, T. J., "The Influence of Laminar Separation and Transition on Low Reynolds Number Airfoil Hysteresis," *Journal of Aircraft*, Vol. 22, No. 9, September 1985, pp. 763–770.

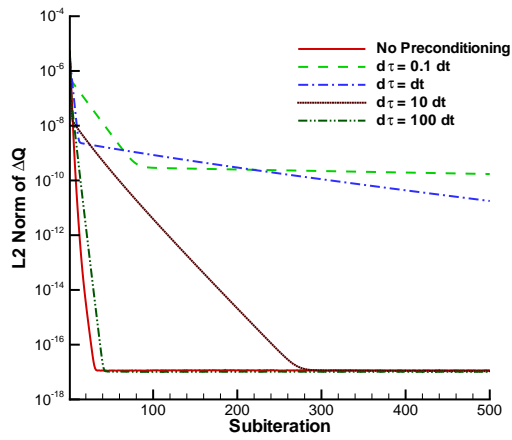
<sup>14</sup>Bohorquez, F., "Rotor Hover Performance and System Design of an Efficient Coaxial Rotary Wing Micro Air Vehicle," *Ph.D. dissertation, Department of Aerospace Engineering, University of Maryland, College Park, MD*, 2007.

<sup>15</sup>Jeong, J. and Hussain, F., "On the Identification of a Vortex," *Journal of Fluid. Mechanics*, Vol. 285, 1995, pp. 69–94.

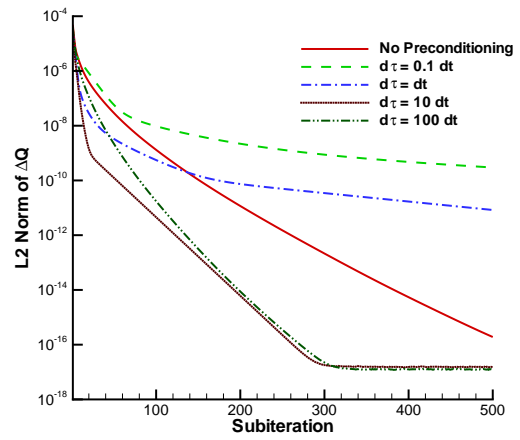
<sup>16</sup>Leishman, J. G., "Principles of Helicopter Aerodynamics," Cambridge University Press, 2002.

<sup>17</sup>Duraisamy, K., Sitaraman, J. and Baeder, J., "High Resolution Wake Capturing Methodology for Accurate Simulation of Rotor Aerodynamics," *61st Annual Forum of the American Helicopter Society*, Grapevine, TX, June 2005.

<sup>18</sup>Lakshminarayan, V. K., and Baeder, J. D., "High Resolution Computational Investigation of Trimmed Coaxial Rotor Aerodynamics in Hover," *Proceedings of the American Helicopter Society International Specialists' Conference on Aeromechanics*, San Francisco, CA, January 2008.

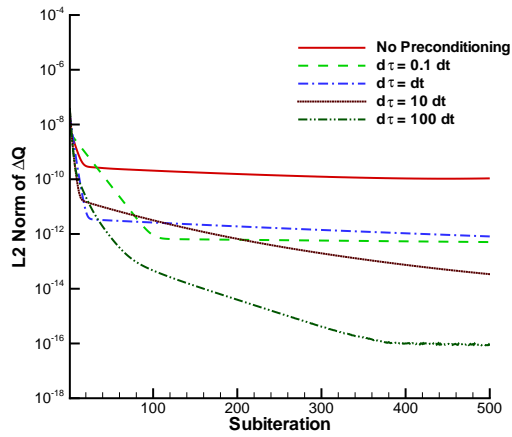


(a)  $CFL_u = 0.1$

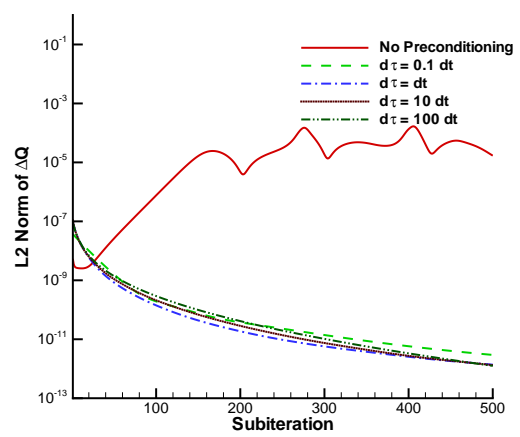


(b)  $CFL_u = 1.0$

Figure 1: Comparison of residual convergence for  $M_\infty = 0.0845$ .



(a)  $CFL_u = 0.1$



(b)  $CFL_u = 1.0$

Figure 2: Comparison of residual convergence for  $M_\infty = 0.000845$ .

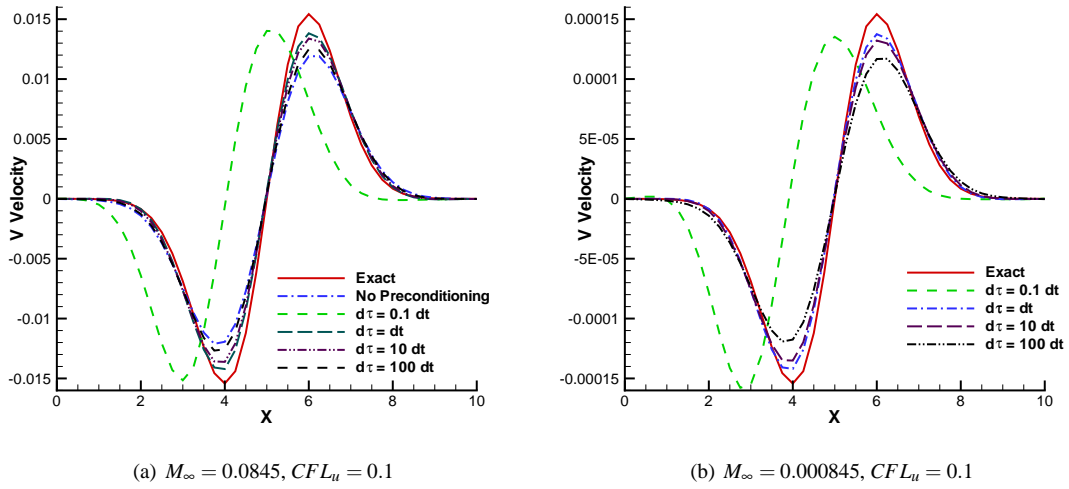


Figure 3: Vertical Velocity profile along  $y = 5$  line.

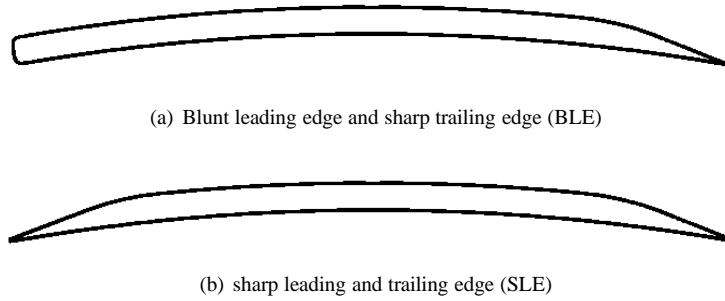


Figure 4: Computational sectional profile.

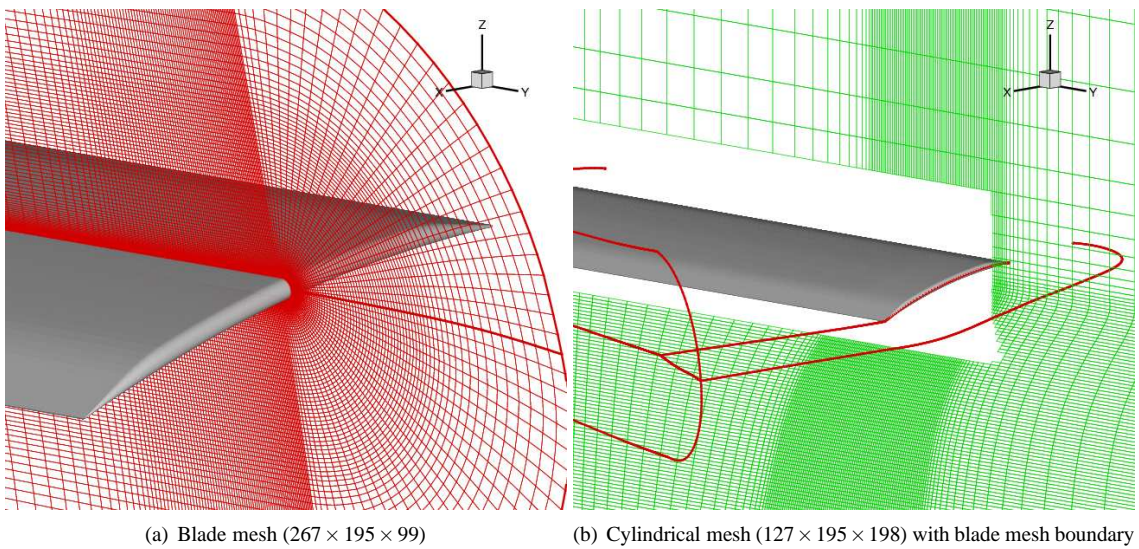
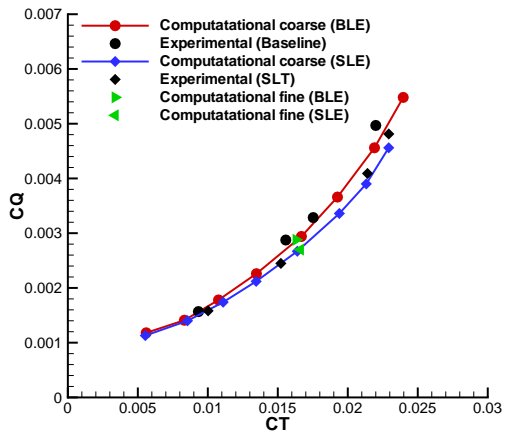
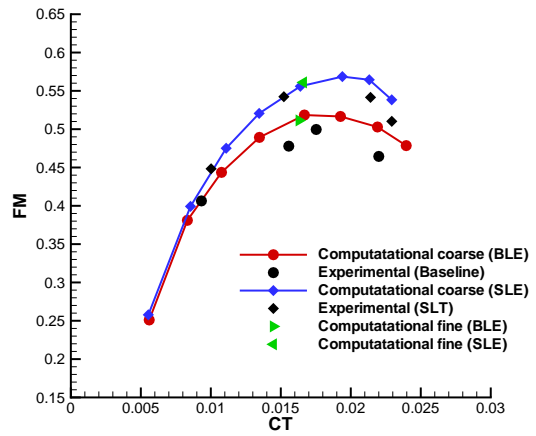


Figure 5: Computational mesh for Micro-rotor calculation.

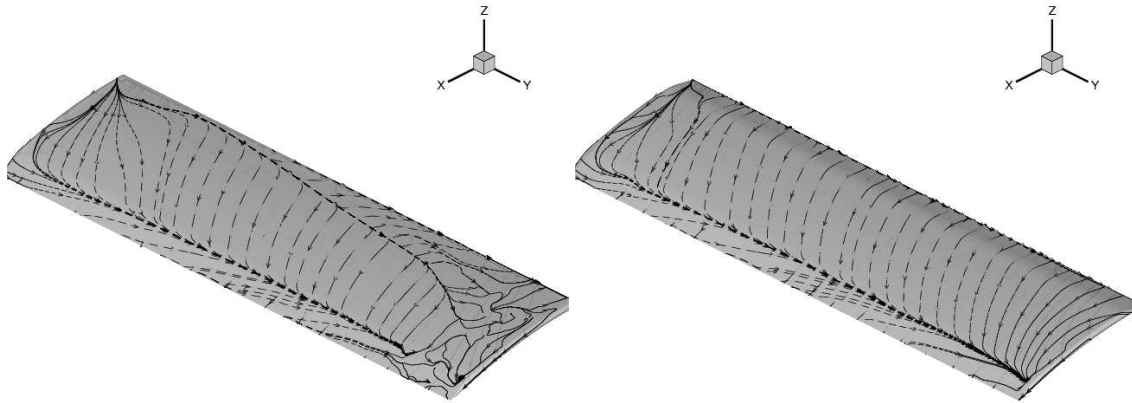


(a)  $C_Q$  vs  $C_T$



(b)  $FM$  vs  $C_T$

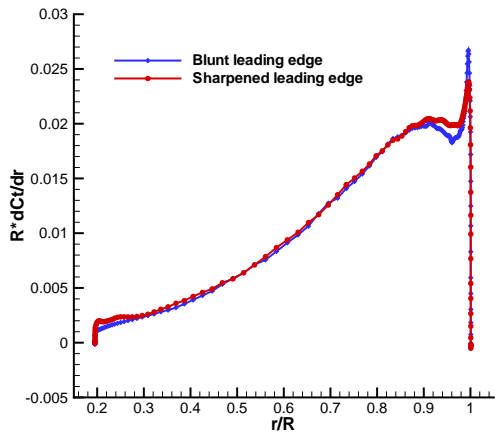
Figure 6: Performance Comparison.



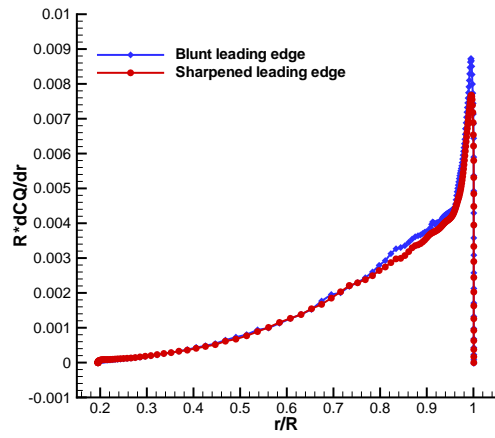
(a) BLE geometry

(b) SLE geometry

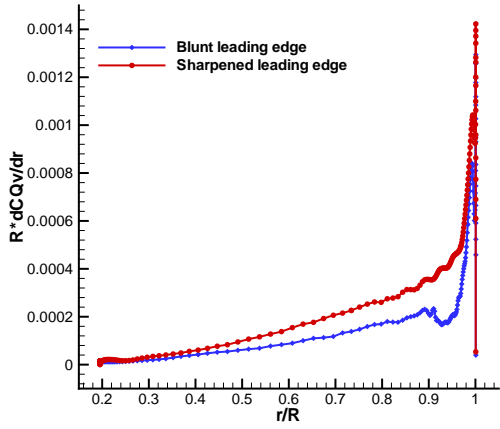
Figure 7: Blade surface streamlines for  $12^\circ$  collective setting.



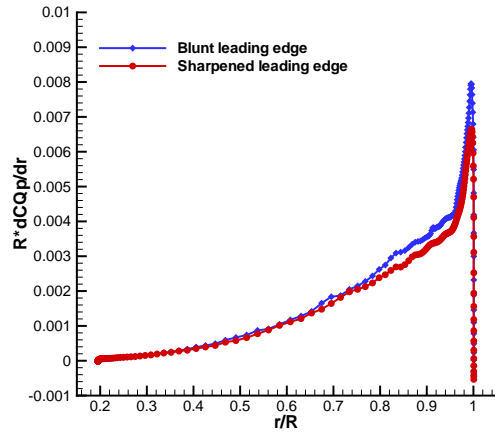
(a) Thrust



(b) Power

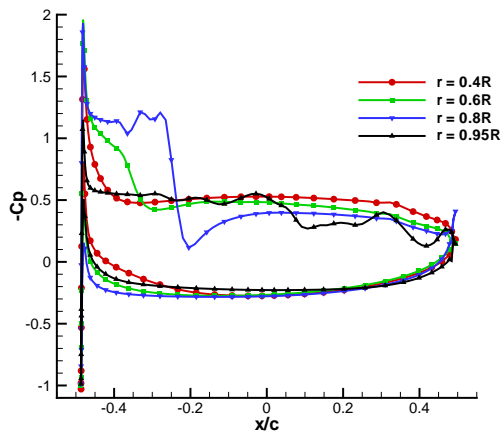


(c) Power due to viscous forces

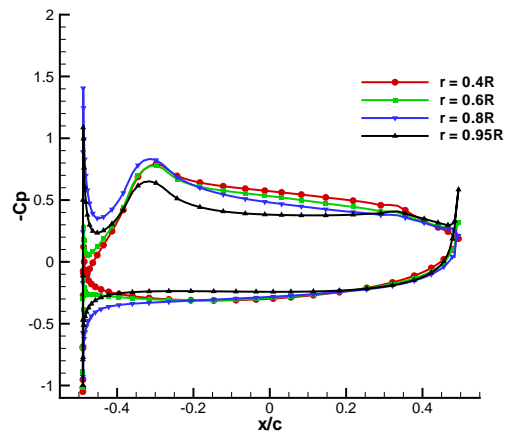


(d) Power due to pressure forces

Figure 8: Spanwise force distribution,  $12^\circ$  collective setting.

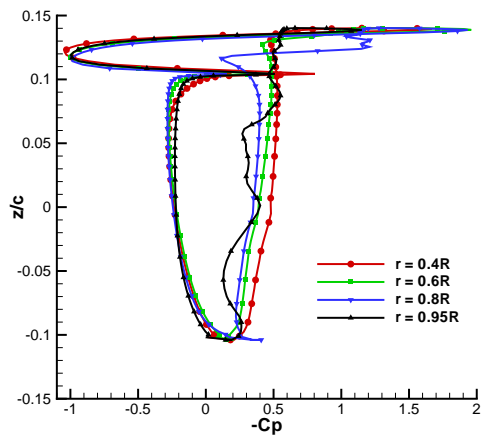


(a) BLE geometry

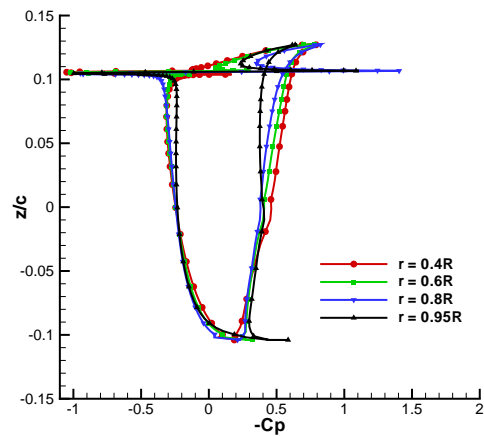


(b) SLE geometry

Figure 9: Blade pressure distribution at different spanwise location,  $12^\circ$  collective setting.

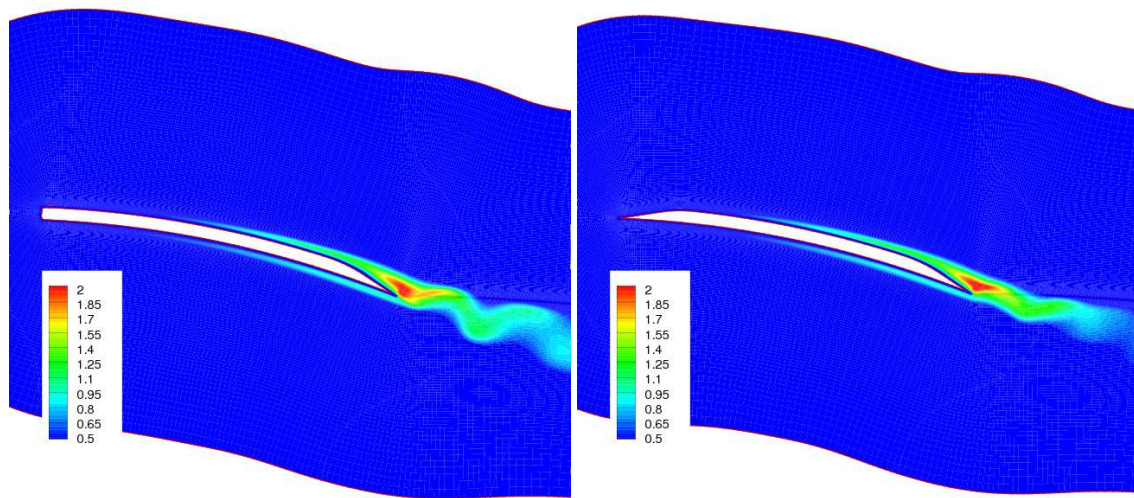


(a) BLE geometry



(b) SLE geometry

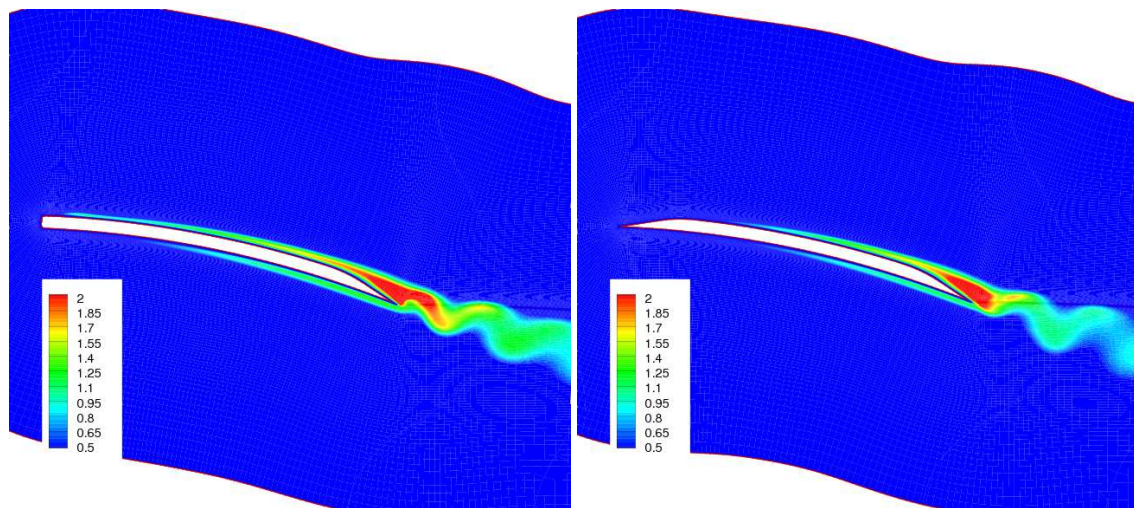
Figure 10: Blade pressure distribution at different spanwise location,  $12^\circ$  collective setting.



(a) BLE geometry

(b) SLE geometry

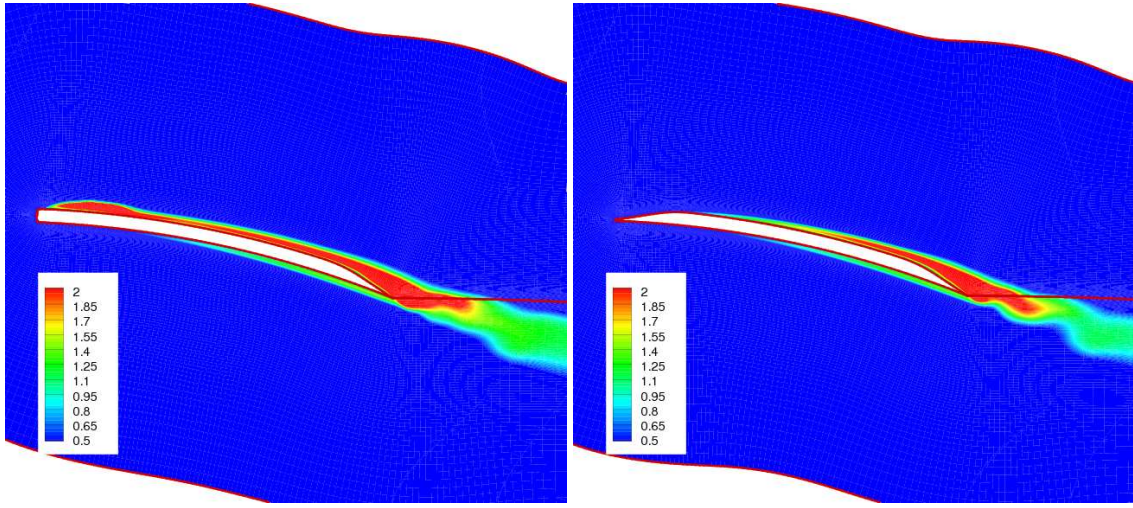
Figure 11: Eddy Viscosity contour at  $0.4R$ ,  $12^\circ$  collective setting.



(a) BLE geometry

(b) SLE geometry

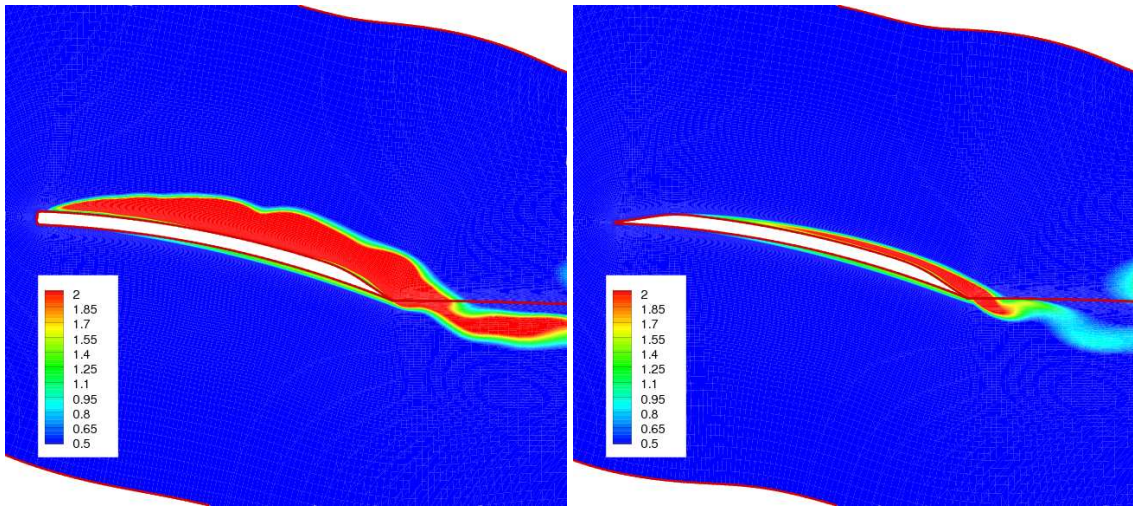
Figure 12: Eddy Viscosity contour at  $0.6R$ ,  $12^\circ$  collective setting.



(a) BLE geometry

(b) SLE geometry

Figure 13: Eddy Viscosity contour at  $0.8R$ ,  $12^\circ$  collective setting.



(a) BLE geometry

(b) SLE geometry

Figure 14: Eddy Viscosity contour at  $0.95R$ ,  $12^\circ$  collective setting.

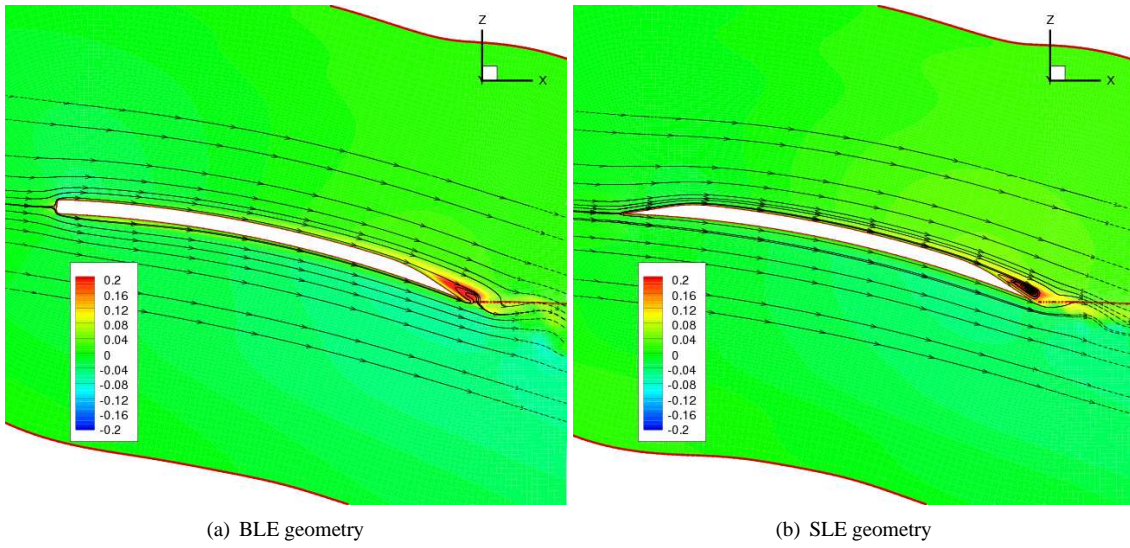


Figure 15: Radial Velocity contour along with streamlines at  $0.4R$ ,  $12^\circ$  collective setting.

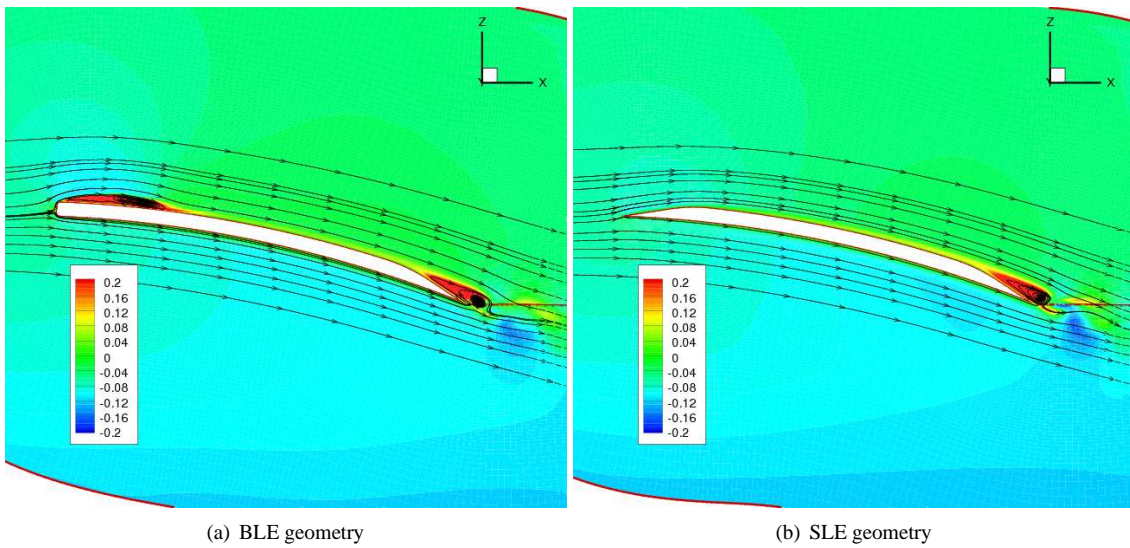


Figure 16: Radial Velocity contour along with streamlines at  $0.8R$ ,  $12^\circ$  collective setting.

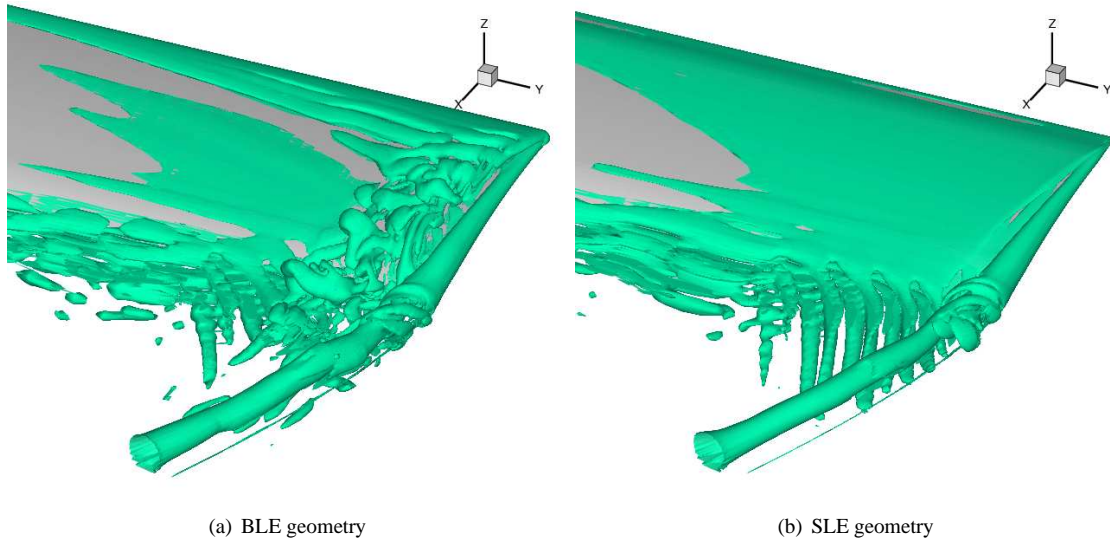


Figure 17: Iso-surfaces of second invariant of velocity magnitude  $q = 8.0$  at  $12^\circ$  collective setting.

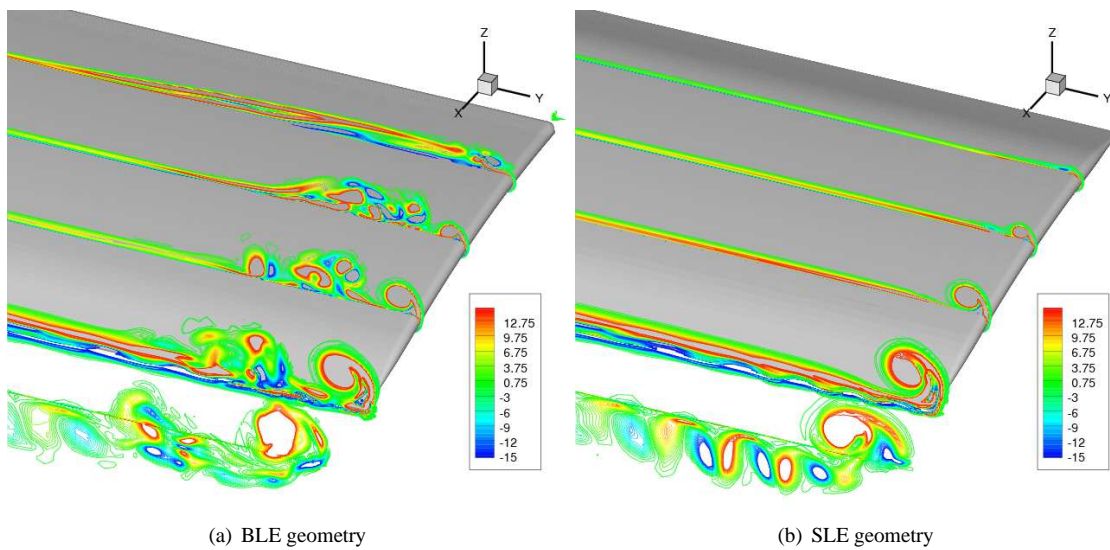


Figure 18: Contours of streamwise vorticity at  $12^\circ$  collective setting.

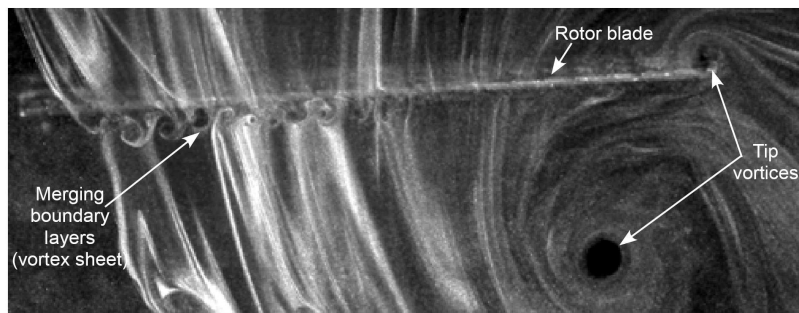


Figure 19: Experimental flow visualization.

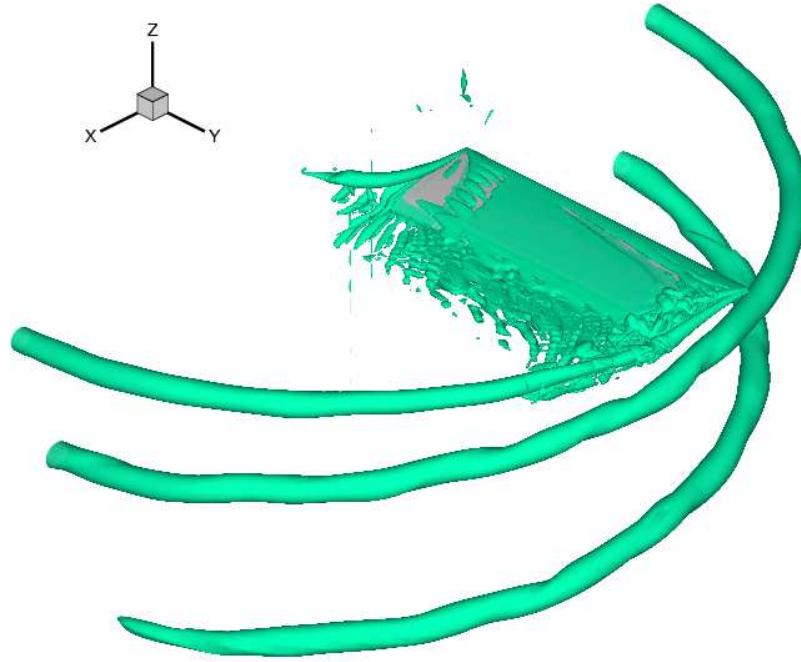
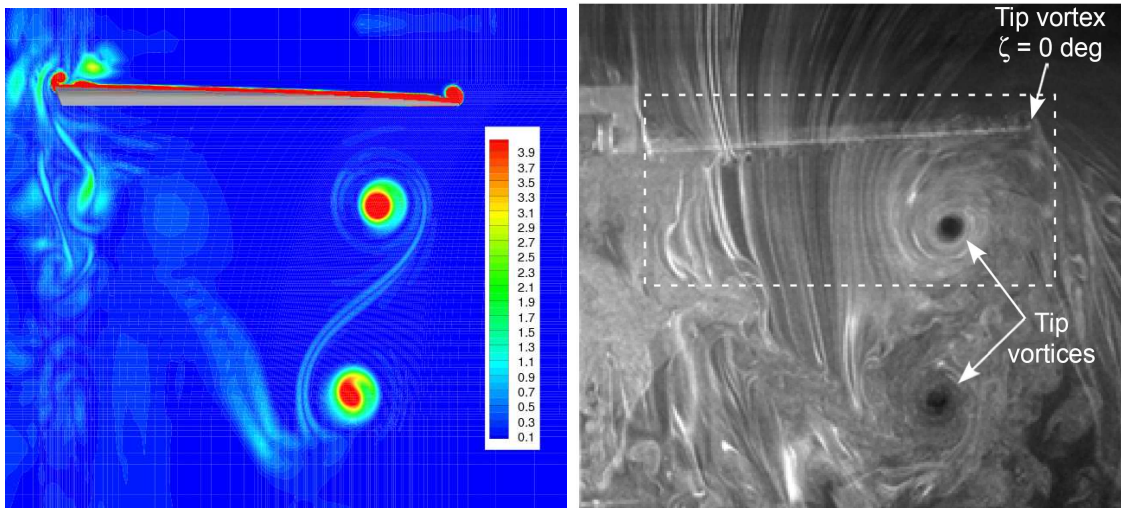


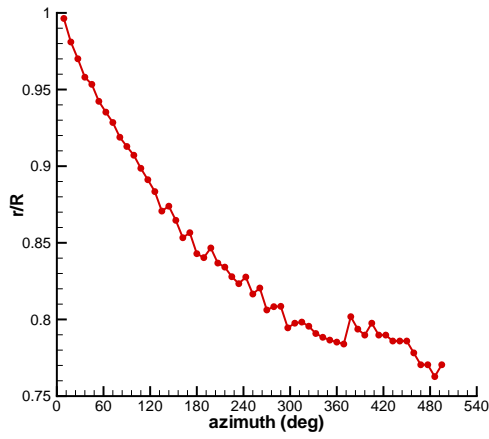
Figure 20: Iso-surfaces of second invariant of velocity magnitude  $q = 1.0$  for BLE geometry at  $12^\circ$  collective setting.



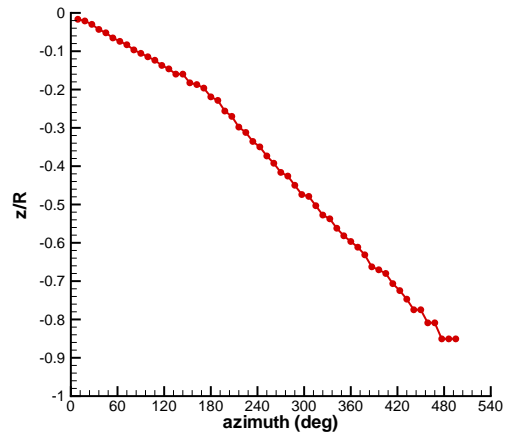
(a) Contours of vorticity magnitude at  $\psi = 0^\circ$  for BLE geometry at  $12^\circ$  collective setting.

(b) Experimental flow visualization

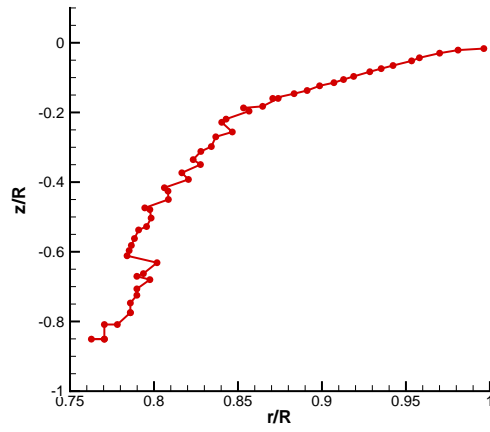
Figure 21: Flow-field comparison.



(a) azimuth vs  $r/R$

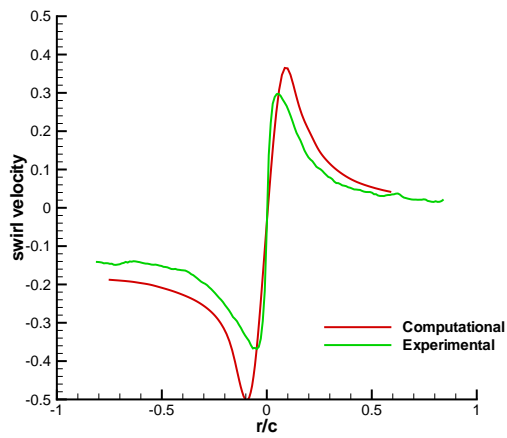


(b) azimuth vs  $z/R$

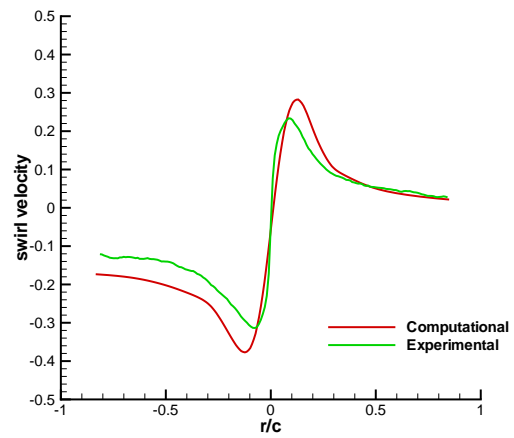


(c)  $r/R$  vs  $z/R$

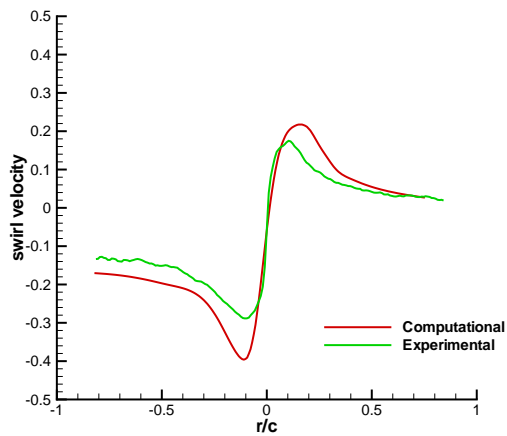
Figure 22: Wake trajectory for BLE geometry at  $12^\circ$  collective setting.



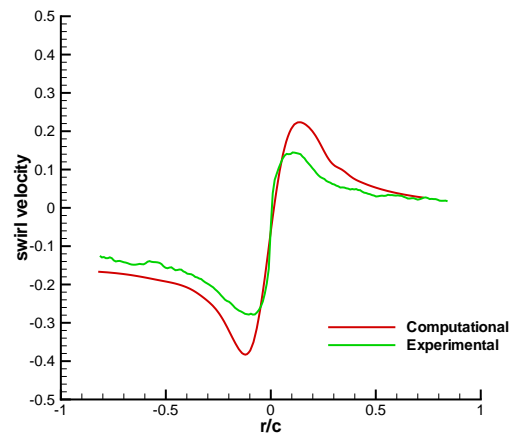
(a)  $\Psi = 30^\circ$



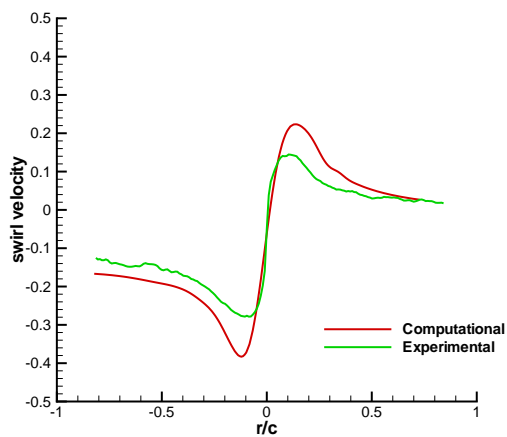
(b)  $\Psi = 60^\circ$



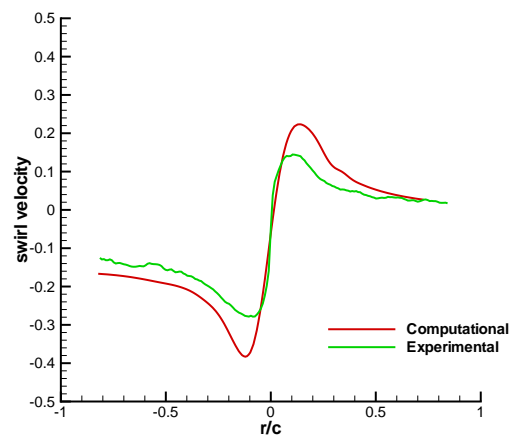
(c)  $\Psi = 90^\circ$



(d)  $\Psi = 120^\circ$

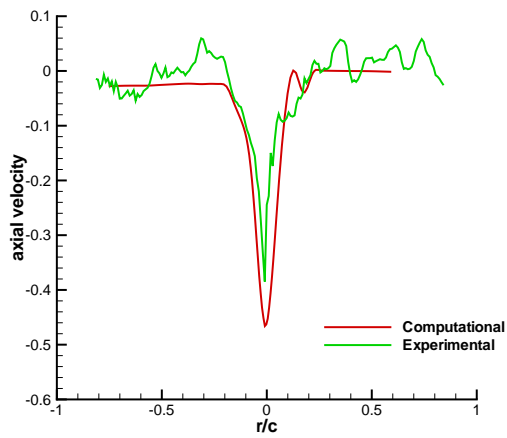


(e)  $\Psi = 150^\circ$

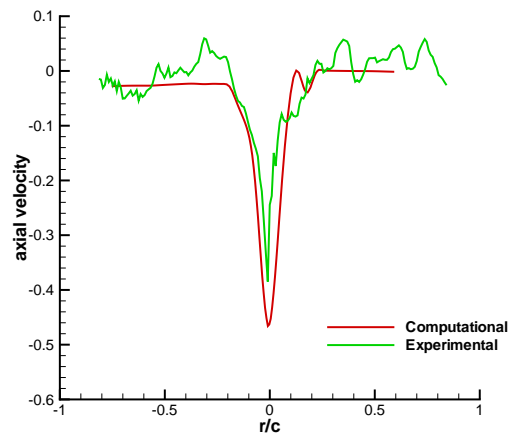


(f)  $\Psi = 180^\circ$

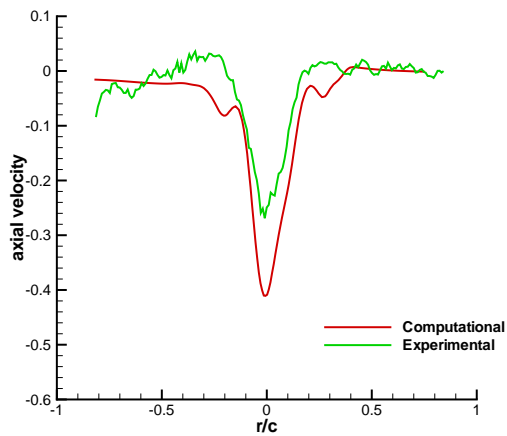
Figure 23: Vortex swirl velocity profile (non-dimensionalized by tip speed) comparison between computational BLE geometry and experimental baseline geometry,  $12^\circ$  collective setting.



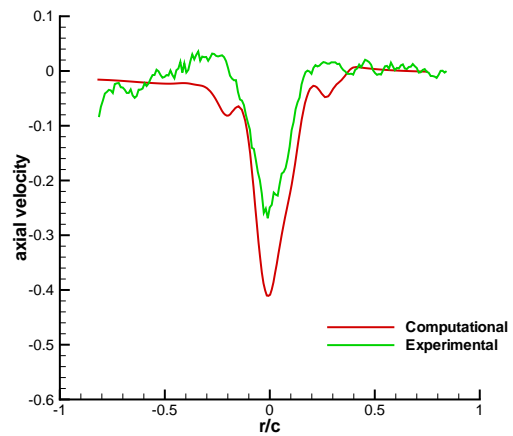
(a)  $\Psi = 30^\circ$



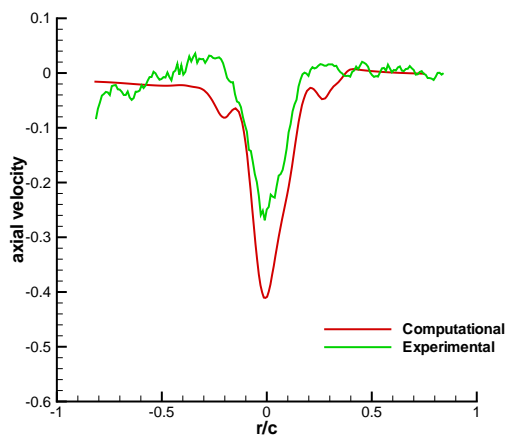
(b)  $\Psi = 60^\circ$



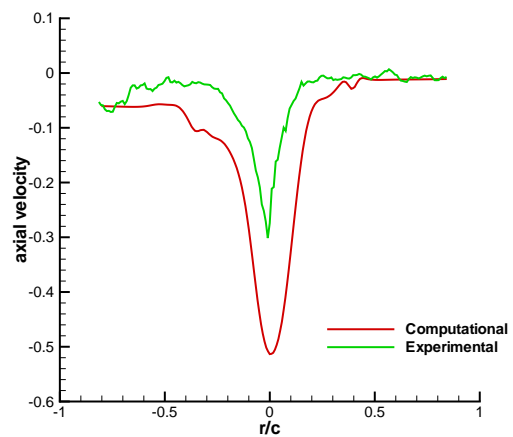
(c)  $\Psi = 90^\circ$



(d)  $\Psi = 120^\circ$

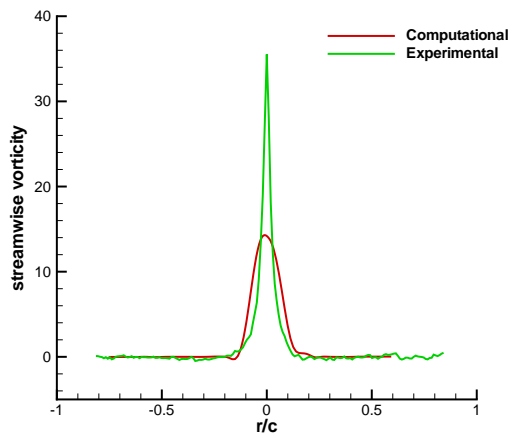


(e)  $\Psi = 150^\circ$

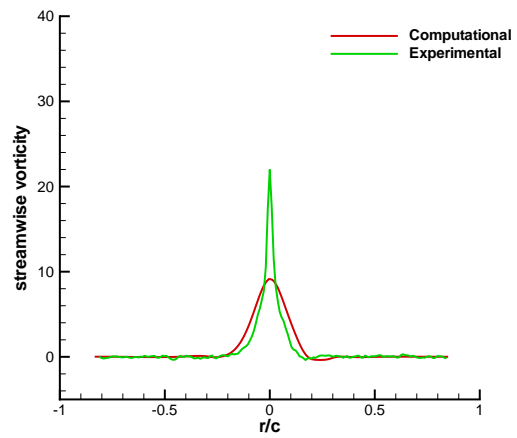


(f)  $\Psi = 180^\circ$

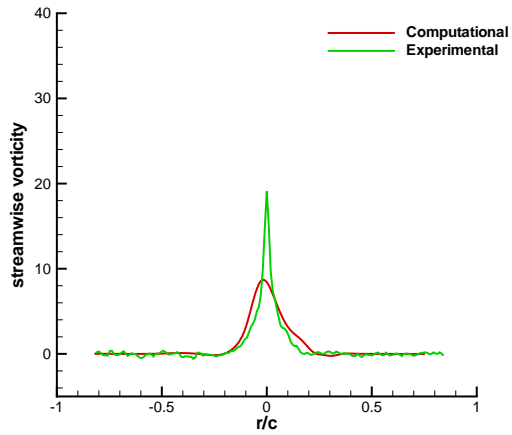
Figure 24: Vortex axial velocity profile (non-dimensionalized by tip speed) comparison between computational BLE geometry and experimental baseline geometry,  $12^\circ$  collective setting.



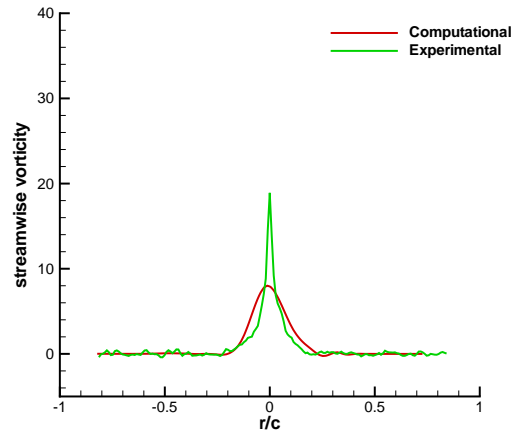
(a)  $\Psi = 30^\circ$



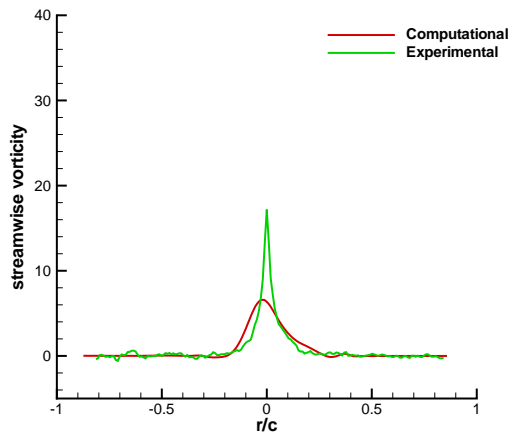
(b)  $\Psi = 60^\circ$



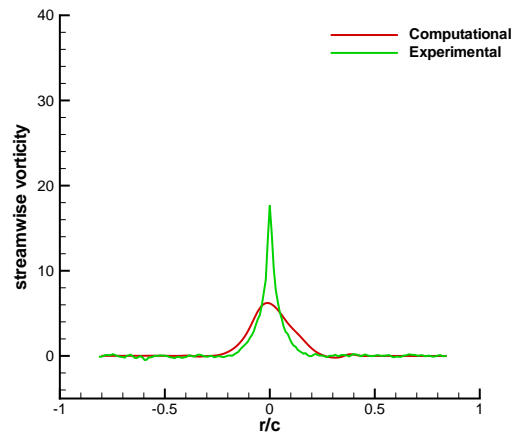
(c)  $\Psi = 90^\circ$



(d)  $\Psi = 120^\circ$

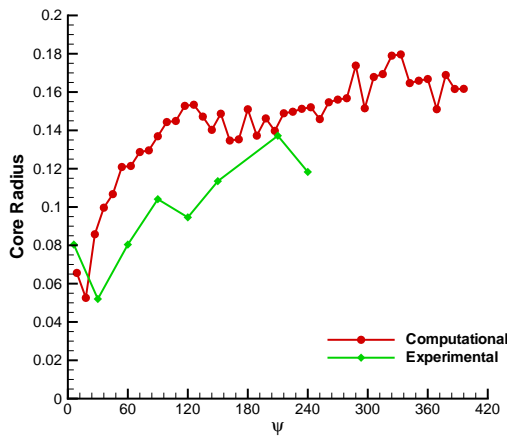


(e)  $\Psi = 150^\circ$

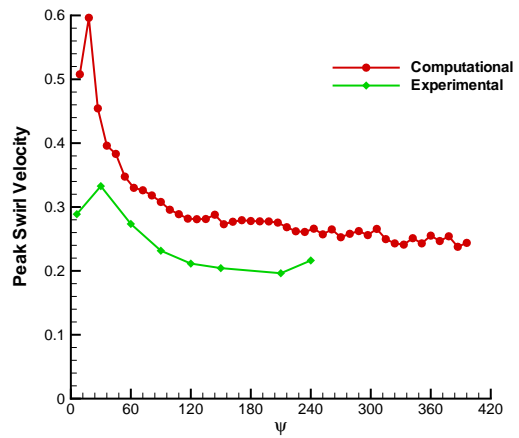


(f)  $\Psi = 180^\circ$

Figure 25: Streamwise vorticity profile (non-dimensionalized by tip speed and blade chord) comparison between computational BLE geometry and experimental baseline geometry,  $12^\circ$  collective setting.

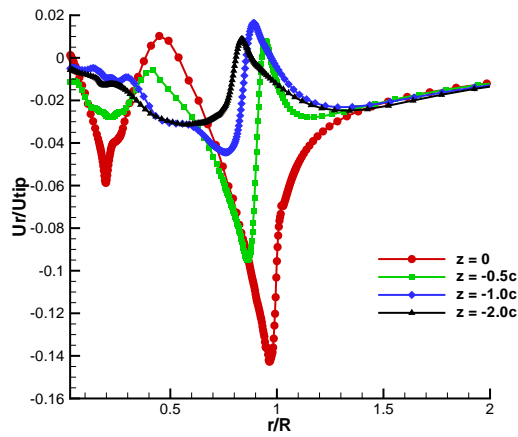


(a)

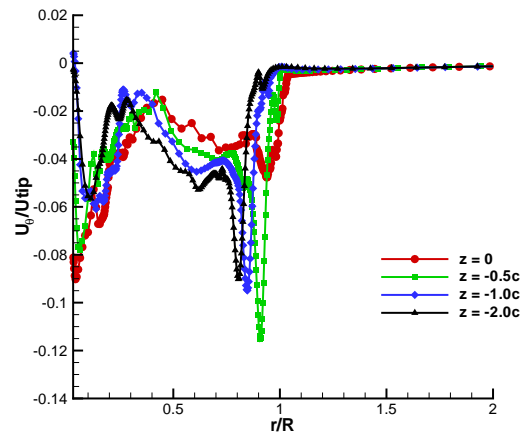


(b)

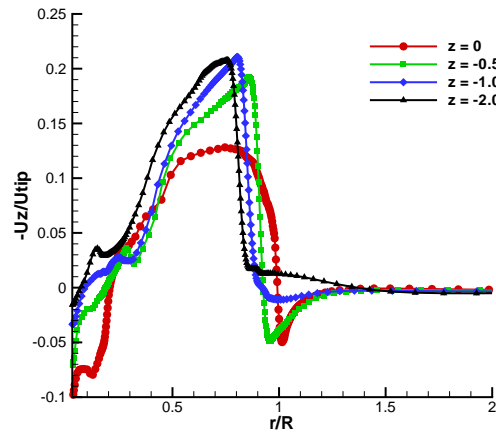
Figure 26: Tip vortex viscous core radius (a) and Peak tip vortex swirl velocity (b) with wake age.



(a) Average radial velocity along span

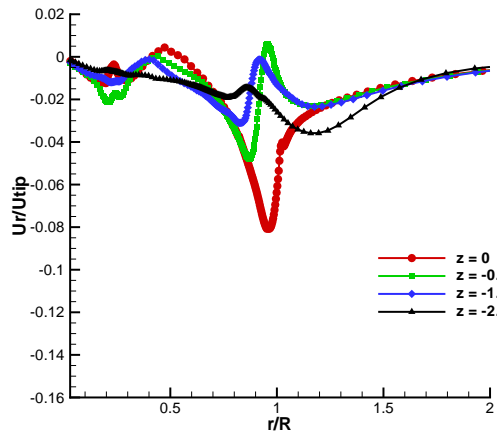


(b) Average swirl velocity along span

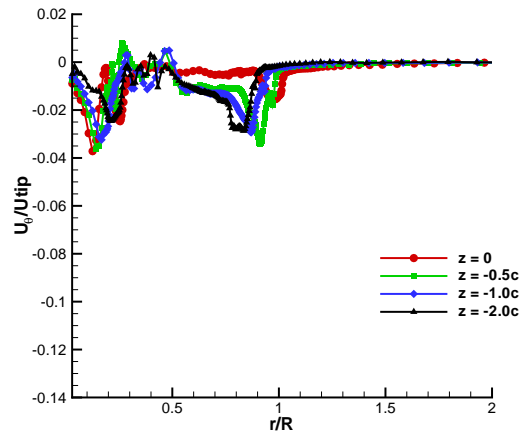


(c) Average inflow velocity along span

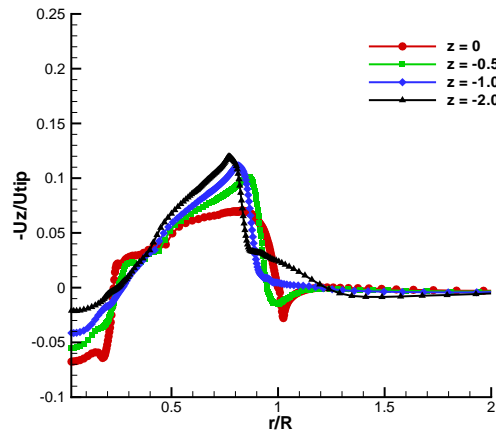
Figure 27: Average velocities along radial direction at different planes below the rotor for BLE geometry at  $12^\circ$  collective setting.



(a) Average radial velocity along span



(b) Average swirl velocity along span



(c) Average inflow velocity along span

Figure 28: Average velocities along span at different planes below the rotor for a full-scale rotor.